

Application of a constrained-transfer-matrix method to metastability in the $d=2$ Ising ferromagnet*

C. C. A. Günther,^{a,b,†,‡} P. A. Rikvold,^{a,b,†,‡} M. A. Novotny^{a,†}

^a Supercomputer Computations Research Institute,
Florida State University, Tallahassee, Florida 32306-4052, USA

^b Department of Physics and Center for Materials Research and Technology,
Florida State University, Tallahassee, Florida 32306-3016, USA

Abstract

Applying a numerical transfer-matrix formalism, we obtain complex-valued constrained free energies for the two-dimensional square-lattice nearest-neighbor Ising ferromagnet below its critical temperature and in an external magnetic field. In particular, we study the imaginary part of the constrained free-energy branch that corresponds to the metastable phase. Although droplets are not introduced explicitly, the metastable free energy is obtained in excellent agreement with field-theoretical droplet-model predictions. The finite-size scaling properties are different in the weak-field and intermediate-field regimes, and we identify the corresponding different critical-droplet shapes. For intermediate fields, we show that the surface free energy of the critical droplet is given by a Wulff construction with the equilibrium surface tension. We also find a prefactor exponent in complete agreement with the field-theoretical droplet model. Our results extend the region of validity for known results of this field-theoretical droplet model, and they indicate that this transfer-matrix approach provides a nonperturbative numerical continuation of the equilibrium free energy into the metastable phase.

1 Introduction

Metastability is commonly observed in a wide variety of systems, ranging from supercooled fluids and vapors [1, 2, 3, 4] to the electroweak [5, 6, 7] and QCD confinement/deconfinement [8, 9] phase transitions, and its description in terms of statistical mechanics has received considerable attention. (See e.g. Refs. [4, 10, 11, 12, 13] for reviews.) Nevertheless, a fully satisfactory microscopic description remains elusive [14]. One characteristic feature of metastable phases is that although they do not fully minimize the free energy, they nevertheless display long-term stability against small perturbations, with lifetimes that can be many orders of magnitude longer than other characteristic timescales of the system [15, 16, 17]. Based on this observation, numerous efforts to formulate a statistical theory of metastability have treated metastable phases as “quasi-equilibrium” phases derived from a constrained partition function that excludes or severely reduces the probabilities of those microstates that are more probable in equilibrium. In the context of a field-theoretical droplet

*Submitted to *Physica A*.

†Partially supported by Florida State University through the Supercomputer Computations Research Institute (U.S. Department of Energy Contract No. DE-FC05-85ER25000) and through Cray Y-MP supercomputer time.

‡Partially supported by the Florida State University Center for Materials Research and Technology and by U.S. National Science Foundation Grants No. DMR-9013107 and DMR-9315969.

model with Fokker-Planck dynamics, these ideas led to the result [18, 19, 20] that the nucleation rate of a metastable phase is proportional to the imaginary part of the analytic continuation of the equilibrium free energy into the metastable phase. However, the original derivation of this result is only valid for large systems in the limit of ultraweak magnetic fields [19, 20], and despite extensive subsequent studies [14, 21, 22, 23, 24, 25, 26, 27, 28], its domain of validity still remains unclear.

In one of these subsequent studies [21], it was suggested that the analytic continuation of the Ising model free energy could be found from certain analytic properties of the eigenvalues of the transfer matrix. Further transfer-matrix work performed on the two-dimensional nearest-neighbor Ising model [22, 23, 24] supported this result. Furthermore, these studies found indications for the existence of an essential singularity at zero magnetic field, as expected from field-theoretical droplet-model calculations [18, 19, 20, 29, 30, 31, 32]. Since then, this result has been confirmed by series expansions [33, 34, 35, 36, 37], exact diagonalization studies [38], Monte Carlo simulations [39, 40], rigorous studies using low-temperature Peierls contours [41], and calculations of two-point correlation functions in a bubble model [42, 43, 44].

Motivated by the transfer-matrix results mentioned above, one of us [45, 46] has introduced a “constrained-transfer-matrix” (CTM) method. It generalizes conventional transfer-matrix (TM) techniques, providing a means to compute complex-valued “constrained free energies” from the eigenvalues and eigenvectors of the transfer matrix. Here we report in detail on the application of the CTM method to a short-range-force model, the two-dimensional ferromagnetic nearest-neighbor Ising model on a square lattice. We find that the imaginary part of the constrained free energy that corresponds to the metastable phase, as obtained by the CTM method, is in excellent agreement with predictions of the field-theoretical droplet model. A brief account of some aspects of this work has been published elsewhere [47].

One alternative approach to the study of metastability is to perform Monte Carlo simulations and measure the lifetime of the metastable phase directly. For the two-dimensional nearest-neighbor Ising ferromagnet this was done in Refs. [22, 48, 49, 50, 51, 52, 53] and more recently in Refs. [54, 55, 56, 57, 58, 59, 60]. We compare this lifetime with the imaginary part of the metastable free energy as obtained by the CTM method and find very similar dependences on the magnetic field, the temperature, and the finite size of the system. This strongly supports the validity of the aforementioned proportionality relation between the nucleation rate and the imaginary part of the metastable free energy.

A comparison of the CTM formalism applied to a short-range-force model, as presented here, and to two- and three-state models with weak long-range forces, presented elsewhere [45, 46, 61, 62, 63], clearly reveals the differences and similarities between these models [64]. The analytic continuation of the equilibrium free energy in long-range-force models has a branch-point singularity at a well-defined non-zero spinodal field [14, 15, 16, 17, 26, 27, 28, 45, 46, 61, 62, 63], whereas it has an essential singularity on the coexistence line at zero magnetic field in short-range-force models [29, 30, 33, 34, 35, 36, 37, 38, 39, 40, 41, 42, 43, 44]. Moreover, whereas long-range-force models exhibit infinitely long-lived metastable phases in the limit of infinite interaction range, short-range-force models display finite, albeit very long lifetimes, even in the thermodynamic limit [22, 48, 49, 50, 51, 52, 53, 54, 55, 56, 57, 58, 59, 60, 65, 66, 67, 68, 69]. However, the results for the imaginary part of the metastable free energy in all of these cases can be explained by assuming that the rate-determining step in the decay process is the creation of a critical excitation whose free-energy cost can be considered as an activation energy.

Our results lead to the conclusion that the CTM formalism provides a method to numerically continue the equilibrium free energy into the metastable region. In contrast to the analytic continuation in field-theoretical droplet models, the CTM formalism does not rely on the explicit introduction of droplets.

The remainder of this article is organized as follows. In Sec. 2 we explain the CTM method and describe the numerical methods used to calculate the eigenvalues and eigenvectors of the TM. Section 3 gives a brief overview of the droplet theory with emphasis on those aspects that are relevant to the interpretation of our results. The numerical results and their interpretation are presented in Sec. 4, followed by a summary and conclusions in Sec. 5.

2 The Constrained-Transfer-Matrix Method

2.1 Theory

We consider the two-dimensional nearest-neighbor Ising ferromagnet on an $N \times L$ lattice at a temperature below its critical temperature T_c . The Hamiltonian is given by

$$\mathcal{H} = -J \sum_{\langle i,j \rangle} s_i s_j - H \sum_i s_i, \quad (1)$$

where $s_i = \pm 1$ denotes the spin at site i , $J > 0$ is the nearest-neighbor coupling, the sums run over all nearest-neighbor pairs and all sites, respectively, and H is the externally applied magnetic field. Throughout this work we use periodic boundary conditions.

The conventional TM method is a technique to calculate standard thermodynamic state functions in equilibrium systems, such as the magnetization, the internal energy, the free energy, and correlation functions [70]. In order to define the TM, one first divides the $N \times L$ lattice into L one-dimensional subsystems of length N . A subsystem configuration $|x_l\rangle$ can be written as a direct product of single-spin configurations in that subsystem: $|x_l\rangle \equiv |s_{1,l}\rangle \cdots |s_{N,l}\rangle$. One then decomposes the total Hamiltonian (e.g. Eq. (1)) into a sum of subsystem Hamiltonians $\bar{\mathcal{H}}$:

$$\mathcal{H} = \sum_{l=1}^L \bar{\mathcal{H}}(x_l, x_{l+1}). \quad (2)$$

The elements of the $2^N \times 2^N$ transfer matrix (TM) \mathbf{T}_0 are then given by

$$\langle x_l | \mathbf{T}_0 | x_{l+1} \rangle = \exp[-\beta \bar{\mathcal{H}}(x_l, x_{l+1})]. \quad (3)$$

Here $\beta = 1/T$ is the inverse temperature with Boltzmann's constant set equal to unity. Using Eqs. (1), (3), and periodic boundary conditions in the L direction, the equilibrium partition function can be written as

$$Z = \text{Tr}(\mathbf{T}_0^L) = \sum_{\alpha} \lambda_{\alpha}^L, \quad (4)$$

where λ_{α} , $0 \leq \alpha \leq 2^N - 1$, denote the eigenvalues of the TM in order of decreasing magnitude. Since \mathbf{T}_0 is finite with all positive elements, the Perron–Frobenius theorem states that the eigenvalue of largest norm, λ_0 , is positive and nondegenerate [70]. Therefore, in the limit $L \rightarrow \infty$, the equilibrium partition function is given by

$$Z = \lambda_0^L. \quad (5)$$

For the equilibrium free-energy density, f_0 , we then obtain

$$f_0 = -\frac{1}{\beta N} \ln \lambda_0. \quad (6)$$

The equilibrium joint and marginal probability densities are given by [70]

$$P_0(x_l, x_{l+k}) = \langle 0 | x_l \rangle \langle x_l | (\lambda_0^{-1} \mathbf{T}_0)^{|k|} | x_{l+k} \rangle \langle x_{l+k} | 0 \rangle \quad (7)$$

and

$$P_0(x_l) = \langle 0|x_l\rangle\langle x_l|0\rangle . \quad (8)$$

In terms of the joint and marginal probability densities, the equilibrium entropy is given by

$$S_0 = -\frac{1}{N} \sum_{x_l, x_{l+1}} P_0(x_l, x_{l+1}) \ln \left[\frac{P_0(x_l, x_{l+1})}{P_0(x_l)} \right] . \quad (9)$$

The CTM formalism [45, 46] extends this scheme to nonequilibrium states by defining constrained probability densities using the orthonormal eigenvectors $|\alpha\rangle$ that correspond to the subdominant eigenvalues of \mathbf{T}_0 :

$$P_\alpha(x_l, x_{l+k}) = \langle \alpha|x_l\rangle\langle x_l|(\lambda_\alpha^{-1}\mathbf{T}_\alpha)^{|k|}|x_{l+k}\rangle\langle x_{l+k}|\alpha\rangle \quad (10)$$

$$P_\alpha(x_l) = \langle \alpha|x_l\rangle\langle x_l|\alpha\rangle . \quad (11)$$

The marginal probability densities, Eq. (11), are normalized and can be interpreted as probability densities of subsystem configurations in a constrained state [21, 22, 23, 24, 25]. It is apparent from Eqs. (7), (8), (10), and (11) that the constrained probability densities reduce to their equilibrium counterparts for $\alpha=0$.

For simplicity, we restrict ourselves in the following discussion to symmetric \mathbf{T}_0 and assume that all its eigenvalues are nondegenerate. (In a large number of cases of physical interest, these conditions are or can be made to be satisfied.) The matrices \mathbf{T}_α are chosen to commute with \mathbf{T}_0 and can hence be expanded in the eigenvectors, $|\beta\rangle$, of \mathbf{T}_0 :

$$\mathbf{T}_\alpha = \sum_{\beta} |\beta\rangle\mu_\beta(\alpha)\langle\beta|. \quad (12)$$

The ‘‘reweighted’’ eigenvalues $\mu_\beta(\alpha)$ are chosen so that \mathbf{T}_α , for $\alpha>0$, has λ_α as its dominant eigenvalue, rather than λ_0 . Furthermore, in order for the entire multi-layer system to be in a uniform state consistent with $P_\alpha(x_l)$, the joint probability densities $P_\alpha(x_l, x_{l+k})$ have to fulfill the following requirements [45]:

1. Stochastic independence at large separation:

$$\lim_{|k|\rightarrow\infty} P_\alpha(x_l, x_{l+k}) = P_\alpha(x_l)P_\alpha(x_{l+k}) , \quad (13)$$

which ensures that fluctuations corresponding to eigenstates orthogonal to $|\alpha\rangle$ decay on a finite length scale. This condition is satisfied if and only if $|\mu_\beta(\alpha)|<|\lambda_\alpha|$ for all $\beta\neq\alpha$.

2. Standard relations between the joint and marginal probability densities:

$$\sum_{x_{l+k}} P_\alpha(x_l, x_{l+k}) = P_\alpha(x_l) , \quad (14)$$

which is satisfied if and only if $\mu_\beta(\alpha)=\lambda_\alpha$ for $\beta=\alpha$.

3. Non-ambiguity of Eqs. (10) and (11) for $k=0$:

$$P_\alpha(x_l, x'_l) = P_\alpha(x_l)\delta_{x_l, x'_l} . \quad (15)$$

This condition requires the matrices \mathbf{T}_α to be of the same rank as \mathbf{T}_0 . It is satisfied if and only if, for all α , $\mu_\beta(\alpha)\neq 0$ for all β for which $\lambda_\beta\neq 0$.

These requirements, however, do not uniquely give the detailed form of \mathbf{T}_α . Since all the $\lambda_\alpha \neq 0$ for the system studied here, a reweighting scheme that satisfies Eqs. (13), (14), and (15), and which was also chosen in Refs. [45, 46, 47, 61, 62, 63], is given by

$$\mu_\beta(\alpha) = \begin{cases} \lambda_\alpha^2/\lambda_\beta & \text{if } |\lambda_\beta| > |\lambda_\alpha| \\ \lambda_\beta & \text{if } |\lambda_\beta| \leq |\lambda_\alpha| \end{cases}. \quad (16)$$

Note that the \mathbf{T}_α for $\alpha > 0$ are in general *not* positive matrices. Since only the eigenvector $|0\rangle$, corresponding to the largest eigenvalue, can be chosen to have all non-negative elements [70], the other eigenvectors, which are orthogonal to $|0\rangle$, necessarily contain some negative and some positive elements. Therefore, at least some of the matrices \mathbf{T}_α for $\alpha > 0$ may not be positive.

In order to define ‘‘constrained’’ state functions, it is convenient to decompose the subsystem Hamiltonian, $\bar{\mathcal{H}}(x_l, x_{l+1})$, into two parts: $\bar{\mathcal{H}}_I$, containing only interaction terms, and $-H\bar{\mathcal{M}}$, containing only terms proportional to the magnetic field. A constrained internal energy per site, U_α , and a constrained field energy, $-HM_\alpha$, can then be defined by replacing the equilibrium probability densities in the expression for the equilibrium expectation values of these quantities with the constrained probability densities. One obtains

$$U_\alpha = \frac{1}{N} \sum_{x_l, x_{l+1}} P_\alpha(x_l, x_{l+1}) \bar{\mathcal{H}}_I(x_l, x_{l+1}) \quad (17)$$

and

$$-HM_\alpha = -\frac{H}{N} \sum_{x_l, x_{l+1}} P_\alpha(x_l, x_{l+1}) \bar{\mathcal{M}}(x_l, x_{l+1}). \quad (18)$$

Constrained entropy densities S_α are defined in analogy with the source entropy of a stationary, ergodic Markov information source (see e.g. [71]):

$$\begin{aligned} S_\alpha &= -\frac{1}{N} \sum_{x_l, x_{l+1}} P_\alpha(x_l, x_{l+1}) \text{Ln} \left[\frac{P_\alpha(x_l, x_{l+1})}{P_\alpha(x_l)} \right] \\ &= -\frac{1}{N} \sum_{x_l, x_{l+1}} P_\alpha(x_l, x_{l+1}) \text{Ln} \langle x_l | \lambda_\alpha^{-1} \mathbf{T}_\alpha | x_{l+1} \rangle. \end{aligned} \quad (19)$$

Since the elements of \mathbf{T}_α are in general not non-negative, this gives rise to an imaginary part in S_α through the principal branch of the complex logarithm $\text{Ln}z = \ln|z| + i\phi$ with $z = |z|e^{i\phi}$ and $-\pi \leq \phi < \pi$. Notice also that for $\alpha=0$, U_α , M_α , and S_α reduce to the corresponding equilibrium quantities.

In analogy with equilibrium thermodynamics, constrained free-energy densities, f_α , are then defined by

$$f_\alpha = U_\alpha - HM_\alpha - \beta^{-1} S_\alpha, \quad (20)$$

which may also be written as

$$f_\alpha = -\frac{1}{\beta N} \ln |\lambda_\alpha| + \frac{1}{\beta N} \sum_{x_l, x_{l+1}} P_\alpha(x_l, x_{l+1}) \text{Ln} \left[\frac{\langle x_l | \mathbf{T}_\alpha | x_{l+1} \rangle}{\langle x_l | \mathbf{T}_0 | x_{l+1} \rangle} \right]. \quad (21)$$

The first term is analogous to the equilibrium case, whereas the second term vanishes in equilibrium. Moreover, the second term is in general complex-valued, since the \mathbf{T}_α are not necessarily positive matrices. Formally, this second term can be considered as a complex generalization of the Kullback discrimination function (see e.g. [72]) for $P_\alpha(x_l, x_{l+1})$ with respect to the divergent ‘probability density’ obtained by substituting \mathbf{T}_0 for \mathbf{T}_α in Eq. (10).

2.2 Numerical methods

In order to calculate any of the constrained free-energy densities in Eq. (20), one needs to know *all* of the 2^N eigenvalues and eigenvectors of the equilibrium transfer matrix \mathbf{T}_0 . The attainable system sizes can be increased considerably by making use of the symmetries of \mathbf{T}_0 (see e.g. [73]). Let X be the 2^N -dimensional vector space with the basis $\{|x_j\rangle\}$ ($j = 1, 2, \dots, 2^N$) of subsystem configurations. The symmetries of \mathbf{T}_0 are represented by unitary operators $\mathbf{U} : X \rightarrow X$ that commute with \mathbf{T}_0 . Applying \mathbf{U} to a particular configuration $|x_j\rangle$ amounts to a permutation of the spins in $|x_j\rangle$. The application of \mathbf{U} to the configurations in X partitions X into subsets, each of which is invariant under \mathbf{U} . Since the number N of spins within a subsystem is finite, \mathbf{U} has a finite period $M \leq N$ with $\mathbf{U}^M = \mathbf{I}$, where \mathbf{I} is the identity in X . This means that the eigenvalues of \mathbf{U} are given by the M roots of unity. Each eigenvalue of \mathbf{U} corresponds to one of the subsets of X .

One can now block-diagonalize \mathbf{T}_0 by writing it in the eigenvector basis of \mathbf{U} , with each block corresponding to a different eigenvalue of \mathbf{U} . The blocks corresponding to the eigenvalues 1 and -1 are called symmetric and antisymmetric, respectively. They are real and symmetric, whereas all the other blocks are Hermitian. Instead of diagonalizing the full $2^N \times 2^N$ transfer matrix all at once, one now diagonalizes each block separately, with the submatrices corresponding to the Hermitian blocks first converted into real symmetric matrices [74].

In our case, \mathbf{T}_0 is symmetric under cyclic permutations \mathbf{P} and reflections \mathbf{R} of the subsystem configurations. Since \mathbf{P} has a period N that in general is larger than the period of \mathbf{R} , we block-diagonalize \mathbf{T}_0 with respect to \mathbf{P} . In order to identify those states that contribute to the metastable phase, we reduce the symmetric block of \mathbf{T}_0 further by block-diagonalizing it again with respect to \mathbf{R} . This exploits the fact that the metastable phase has the same symmetry as the stable phase, which is symmetric under both \mathbf{P} and \mathbf{R} [22, 23, 24].

The diagonalization is performed in two steps. First, we reduce the matrices to tridiagonal form by the Householder method, and then we use a QL algorithm with implicit shifts to find the eigenvectors and eigenvalues of the resulting tridiagonal matrices [74].

Finally, in order to calculate the constrained free-energy densities we transform the eigenvectors of the transfer matrix, which are now written in terms of the basis in which \mathbf{T}_0 is block-diagonal, back into the basis $\{|x_j\rangle\}$ ($j = 1, \dots, 2^N$) of subsystem configurations. The unitary transformation to accomplish this is constructed from the eigenvectors of \mathbf{P} and \mathbf{R} [75].

It turns out that the imaginary parts of the metastable constrained free-energy densities are extremely small (as will be seen later in Fig. 3(b)), although the magnitude of each individual term in the sum of Eq. (21) may be on the order of unity. In order to attain sufficient precision, the diagonalization was therefore performed in 128-bit precision on a Cray Y-MP/432 vector supercomputer. The total computer time spent in this study was on the order of 1000 CPU hours.

For temperatures $T/J \leq 0.4$, the limit on the attainable system sizes is given by numerical underflow for small $|H|$, preventing us from studying system sizes larger than $N=9$ for $T/J=0.4$. For all higher temperatures studied, the maximum system size attainable is $N=10$, limited by the available computer memory.

3 Droplet Theory

Suppose we prepare the system with $H < 0$, so that its average magnetization is close to -1 , and then quench the field through $H=0$ to a value $H > 0$, such that the average magnetization is approximately unchanged. This state is then no longer a global minimum of the free energy. Nevertheless, it might persist for a period of time many orders of magnitude longer than other characteristic timescales of the system [15, 16, 17]. This can be used as an operational definition of metastability.

Starting with the Becker–Döring droplet model [10, 11], one assumes that the decay of metastable phases proceeds through the spontaneous formation of droplets of up spins in the background of down spins. Assuming further that the distance between droplets is much larger than their characteristic size (which is reasonable for sufficiently low temperatures and weak fields [57, 76, 77]), one can treat them as a gas of noninteracting droplets. (In the following, we always assume that H is sufficiently weak, so that interactions between droplets are negligible.) The probability of creating a droplet is then proportional to the Boltzmann factor $e^{-\beta F_D}$, where F_D is the free energy of the droplet. The final assumption of the Becker–Döring droplet model is that F_D is given by the sum of the surface free energy and the bulk free energy of the droplet. If the surface free energy does not change with H and is an increasing and convex function of the volume V of the droplet, and if the bulk free energy is a decreasing function of H and V then a critical droplet with volume V_c exists so that droplets with $V > V_c$ tend to grow, leading to the decay of the metastable phase. It also follows that V_c increases with decreasing H . The quantity V_c can be obtained by maximizing F_D .

3.1 Infinite systems

We assume for the moment that the system is infinitely large. We then express the surface free energy, Σ , in the form $\Sigma = V^{\frac{d-1}{d}} \widehat{\Sigma}$, where d is the spatial dimension, and we denote the difference between the bulk free-energy densities of the metastable and the stable phase by Δf . Then F_D can be written as

$$F_D = V^{\frac{d-1}{d}} \widehat{\Sigma} - V \Delta f. \quad (22)$$

Maximizing F_D yields

$$V_c = \left(\frac{(d-1)\widehat{\Sigma}}{d\Delta f} \right)^d. \quad (23)$$

Let $\Delta m \equiv m_{\text{ms}} - m_{\text{st}}$, where m_{ms} and m_{st} denote the magnetizations of the metastable and stable phases, respectively. The approximation $\Delta f \approx |H| \Delta m$ incorporates the effects of droplet nesting, which becomes increasingly important as the temperature increases from zero to T_c [37]. Inserting $|H| \Delta m$ and Eq. (23) into Eq. (22), the free-energy cost of the critical droplet, $F_c(T, H)$, is obtained as

$$F_c(T, H) = \left(\frac{\widehat{\Sigma}}{d} \right)^d \left(\frac{d-1}{|H| \Delta m} \right)^{d-1}. \quad (24)$$

Within the context of the droplet model, the nucleation rate of critical droplets per unit volume is proportional to the probability of creating a critical droplet and can hence be written in the form [10, 11, 19, 20]

$$I(T, H) = I_0(T, H) e^{-\beta F_c(T, H)} = I_0(T, H) \exp \left(-\frac{\beta \Xi}{|H|^{d-1}} \right) \quad (25)$$

with

$$\Xi = \left(\frac{\widehat{\Sigma}}{d} \right)^d \left(\frac{d-1}{\Delta m} \right)^{d-1}. \quad (26)$$

The proportionality factor $I_0(T, H)$ in Eq. (25) can be derived by going beyond the Becker–Döring droplet model to a field-theoretical droplet model with Fokker-Planck dynamics. Within this framework it has been shown [18, 19, 20] that for infinitely large systems in ultraweak fields, the nucleation rate per unit volume is proportional to the imaginary part of a complex-valued

“constrained” free-energy density, $\text{Im}f_{\text{ms}}$, obtained by analytic continuation of the equilibrium free energy into the metastable phase [19, 20]:

$$I(T, H) = \frac{\beta\kappa}{\pi} |\text{Im}f_{\text{ms}}|. \quad (27)$$

Here κ is a kinetic prefactor which depends on the details of the dynamics, and the imaginary part of the constrained free-energy density is given by [18, 31]

$$|\text{Im}f_{\text{ms}}| = B(T)|H|^b \exp\left(-\beta F_c(T, H) \left[1 + O(H^2)\right]\right), \quad (28)$$

Inserting $F_c(T, H)$ from Eq. (24) into Eq. (28), one obtains

$$|\text{Im}f_{\text{ms}}| = B(T)|H|^b \exp\left(-\frac{\beta\Xi}{|H|^{d-1}} \left[1 + O(H^2)\right]\right), \quad (29)$$

where Ξ is given by Eq. (26). The function $B(T)$ is expected to be nonuniversal, whereas the exponent b is universal and related to surface excitations (Goldstone modes) of the critical droplet [18, 31]:

$$b = \begin{cases} (3-d)d/2 & \text{for } 1 < d < 5, \ d \neq 3 \\ -7/3 & \text{for } d=3 \end{cases}. \quad (30)$$

Omitting the surface excitations in the derivation of Eq. (29) leads to [78]

$$b = -1 - \frac{(d-1)d}{2}. \quad (31)$$

There is strong numerical evidence that $b=1$ for $d=2$ [33, 37, 57, 79], in agreement with Eq. (30) and disagreement with Eq. (31).

Under the assumption that the critical droplet is sufficiently compact, one can define its “radius” R_c as half of its spanning length along one of the primitive lattice vectors. One can then write

$$V_c = \Omega_d R_c^d, \quad (32)$$

where Ω_d incorporates the detailed shape of the droplet. Using Eq. (23) this leads to

$$R_c = \frac{(d-1)\widehat{\Sigma}}{d\Omega_d^{1/d}\Delta f}. \quad (33)$$

Making the additional assumption that the critical droplet shape can be obtained from a Wulff construction with an anisotropic surface tension, one can relate the shape factor Ω_d to the surface tension. Let $\sigma(\hat{n})$ be the anisotropic surface tension of an interface with normal \hat{n} . In the Wulff construction one first draws a polar plot of the surface tension. According to Wulff’s theorem, the shape of the droplet is then given by the inner envelope of the geometric construction obtained by drawing a line tangential to the polar plot of $\sigma(\hat{n})$ for each direction \hat{n} , i.e. [80, 81, 82, 83, 84]

$$\lambda R(\hat{r}) = \min_{\hat{n}} \frac{\sigma(\hat{n})}{\hat{n} \cdot \hat{r}}. \quad (34)$$

Here $R(\hat{r})$ is the length of the radius vector in the direction \hat{r} , and λ is a scale factor to be determined from the actual size of the droplet.

If W denotes the volume bounded by $R(\hat{r})$, as given by Eq. (34) with $\lambda=1$, then the total surface free energy of the droplet is given by $\Sigma=dW^{1/d}V^{(d-1)/d}$ [81]. With $\Sigma=\widehat{\Sigma}V^{(d-1)/d}$, this leads to

$$W = \left(\frac{\widehat{\Sigma}}{d} \right)^d. \quad (35)$$

Furthermore, in the Wulff construction with $\lambda=1$, the length of the radius vector of W in any direction is the surface tension in that direction. Therefore W and V_c are related by $V_c=(R_c/\sigma_0)^dW$, where σ_0 denotes the surface tension in one of the symmetry directions. Combining this with Eqs. (32) and (35), one obtains

$$\Omega_d = \left(\frac{\widehat{\Sigma}}{d\sigma_0} \right)^d, \quad (36)$$

so that the radius of the critical droplet from Eq. (33) is given by the standard relation

$$R_c = \frac{(d-1)\sigma_0}{\Delta f}, \quad (37)$$

which, using $\Delta f \approx |H|\Delta m$, can also be written as

$$R_c = \frac{(d-1)\sigma_0}{|H|\Delta m}. \quad (38)$$

The size of a critical droplet therefore increases with decreasing $|H|$, and its shape changes from a square at low temperatures to a circle near T_c .

3.2 Finite systems

For $N^{d-1} \times \infty$ hypercylindrical systems of finite transverse extent N , several distinct field regions can be distinguished: an intermediate-field region, where $R_c \ll N$; a small-field region, where $R_c \gtrsim N$; and $H=0$, where both phases coexist. (We do not here discuss the strong-field region, where droplet interactions must be taken into account.)

For $R_c \ll N$, finite-size effects are negligible, so the decay rate of the metastable phase does not depend on N . All the results derived in Sec. 3.1 therefore apply in the intermediate-field regime. For $R_c \gtrsim N$, on the other hand, finite-size effects have to be taken into account. This weak-field region coincides with the region of validity of finite-size scaling at first-order phase transitions described in Refs. [85, 86, 87].

We restrict the following discussion to $d=2$. It has recently been shown rigorously [88, 89, 90, 91] that for very low temperatures and $|H|/J < 4$, a large metastable Ising ferromagnet in two dimensions with local Metropolis dynamics decays through a single nucleating droplet of the shape shown in Fig. 1(a). This is an $(l_c-1) \times l_c$ rectangle of overturned spins with a single additional overturned spin as a “knob” on one of its long sides. The length $l_c = \lceil 2J/|H| \rceil$ is the smallest integer larger than $2J/|H|$, where $2J/|H| = \lim_{T \rightarrow 0} 2R_c$. Flipping the remaining l_c-1 spins on the side with the “knob” results in a net gain of energy, and the resulting $l_c \times l_c$ droplet is the low-temperature, discrete-lattice equivalent of the critical droplet discussed in Sec. 3.1. Finite-size effects due to the possibility of subcritical droplets wrapping around the lattice in the transverse direction are to be expected for $l_c \geq N-1$ or (extrapolating in an approximate fashion to nonzero T) $2R_c > N-2$, which yields $|H| < 2\sigma_0/[(N-2)\Delta m] \leq 2J/(N-2) \equiv H_2$.

However, critical droplets of equilibrium shape are not the only configurations comparable to the system size that may nucleate the stable phase by wrapping around the lattice. It is easy to

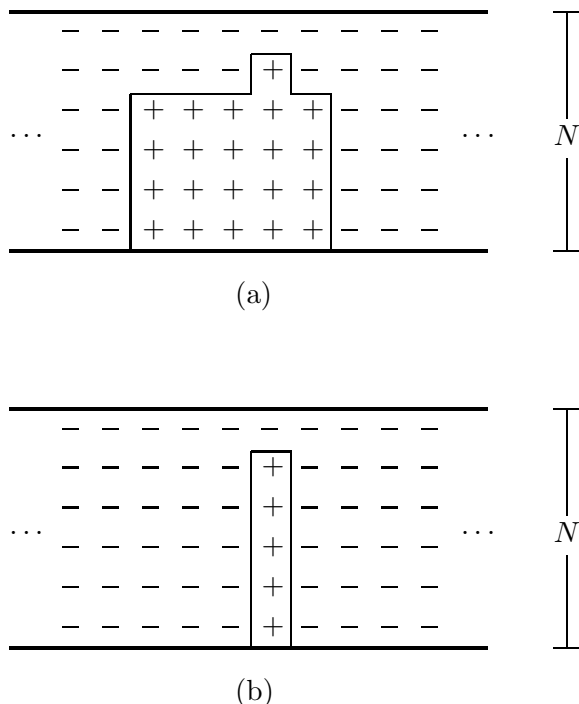


Figure 1: Sketch of two critical excitations that contribute to the decay of the metastable phase at weak positive fields and low temperatures. Configurations shaped like the one depicted in (a) dominate for $|H| \gtrsim H_2 = 2J/(N-2)$. The “rod”-like configuration shown in (b) prevails for $|H| \lesssim H_1 = 2J/(N-1)$. See details in Sec. 3.2.

show that for $|H| < H_2$, still lower-energy configurations that are capable of spanning the system by flipping only one single spin can be constructed by successively removing one layer of + spins from one of the short sides of the droplet shown in Fig. 1(a), until one reaches the $(N-1) \times 1$ “rod”-shaped cluster shown in Fig. 1(b). For $H_2 > |H| > 2J/(N-1) \equiv H_1$, a further energy reduction can be achieved by adding $(N-1) \times 1$ slices back onto one of the long sides of the cluster in Fig. 1(b), until one reaches an $(N-1) \times (N-1)$ cluster. This does not hold true for $|H| < H_1$. Here the “rod”-shaped cluster of Fig. 1(b) is the lowest-energy configuration that can nucleate the stable phase by flipping a single spin.

The above observations lead to the following predictions for the finite-size scaling of $|\text{Im}f_{\text{ms}}|$. For $|H| > H_2$, finite-size effects should be negligible, for $H_1 < |H| < H_2$ the behavior should be rather complicated due to the large number of competing clusters with nearly degenerate energies, and for $|H| \lesssim H_1$ the behavior should be determined by “rod”-shaped clusters like the one shown in Fig. 1(b).

To leading order, the free-energy cost F_c of creating the “rod”-shaped critical cluster in Fig. 1(b) is given by its surface free energy only, so that $F_c \approx 2\sigma(T, H)N$. In analogy with the equilibrium surface tension, $\sigma(T, H)$ here denotes the “surface tension” of the critical droplet at non-zero fields. Inserting F_c into Eq. (28), one obtains

$$|\text{Im}f_{\text{ms}}| \propto e^{-2\beta\sigma(T, H)N}. \quad (39)$$

The largest corrections to Eq. (39) should include a bulk term in the exponential, which is of

the form $-2|H|(N-1)$ for the particular critical excitation considered here, and an N -dependent prefactor.

In the infinite-system limit $H_2 \rightarrow 0$. We then expect that $\sigma(T, H) \rightarrow \sigma_{\text{eq}}(T)$ for large N , where $\sigma_{\text{eq}}(T)$ is the exact equilibrium surface tension as obtained from Onsager's solution of the two-dimensional Ising model [81, 82, 85].

At $H=0$ one can show (see Appendix A) that $|\text{Im}f_{\text{ms}}|$ as defined in the CTM formalism, Eq. (20), is given by

$$|\text{Im}f_{\text{ms}}| \propto (N\xi_N)^{-1}. \quad (40)$$

Here, $\xi_N \equiv \ln|\lambda_0/\lambda_1|$ denotes the correlation length which at $H=0$ is [85, 86, 87]

$$\xi_N \propto N^{1/2} e^{\beta\sigma_{\text{eq}}(T)N}, \quad (41)$$

with a nonuniversal proportionality constant [86]. Inserting Eq. (41) into Eq. (40) one obtains

$$|\text{Im}f_{\text{ms}}| \propto N^{-3/2} e^{-\beta\sigma_{\text{eq}}(T)N}. \quad (42)$$

Note that the coefficient of σ_{eq} in Eqs. (39) and (42) differ by a factor of two. Physically, this corresponds to the fact that, whereas the rod-like droplets that dominate for $|H| \lesssim H_1$ correspond to pairs of tightly bound transverse interfaces, the interfaces are unbound for $H=0$ [86].

4 Numerical Results and Discussion

Since the metastable phase has the same symmetry as the stable phase [22, 23, 24], which is symmetric under cyclic permutations and reflections, we consider only those eigenstates of the TM that are symmetric under cyclic permutations and reflections. As an example, in Fig. 2 we plotted the eigenvalue spectrum as $-\ln\lambda_\alpha/(\beta N)$ (Fig. 2(a)), which corresponds to the first term in Eq. (21), and the constrained magnetizations (Fig. 2(b)) for $T/J=1.0$ ($T/T_c=0.44068\dots$) and $N=8$. When the eigenvalue spectrum is plotted as in Fig. 2(a), the branch corresponding to $\alpha=0$ is the equilibrium free-energy density, Eq. (6). In Fig. 2(b), it corresponds to the branch with magnetization close to $+1.0$.

As seen in Fig. 2(a), for weak magnetic fields, certain eigenvalues group together into fans. In order to identify which eigenvalues correspond to which subsystem configurations, we calculated for $T=0$ the internal energies, U_α , and the magnetization, M_α , for all those subsystem configurations that are symmetric under cyclic permutations and reflections. Configurations with the same number of interfaces parallel to the transfer direction have the same value of U_α . We also find that at $H=0$ and $T>0$, the averages calculated over all those $-\ln\lambda_\alpha/(\beta N)$ that belong to the same fan are nearly equal to the $T=0$ values of U_α . (For example for $N=10$ and $T/J=1.0$, the discrepancies between U_α and the corresponding averages are smaller than 2%.) We therefore conclude that all the eigenvalues that belong to the same fan correspond to subsystem configurations with the same number of interfaces. The absence of exact degeneracies between the eigenvalues that belong to the same fan for $T>0$ is an entropy effect. Finally, we find that away from the crossings, the negative of the slopes of the $-\ln\lambda_\alpha/(\beta N)$ are approximately given by the magnetizations M_α (with discrepancies that are again smaller than 2%).

In accordance with earlier transfer-matrix studies [21, 22, 23, 24, 25, 61, 62, 63, 64, 92], the eigenstate $|\alpha\rangle$ corresponding to the metastable phase at a given field was identified as the one with the largest magnetization opposite in direction to the magnetic field (marked by a thick solid line in Fig. 2 in the field region where this $-\ln\lambda_\alpha$ is not the uppermost branch). As was already observed

previously [22], such an eigenstate can be identified. Furthermore, the metastable eigenvalues vary little with N , indicating the existence of a well-defined thermodynamic limit for that state [22].

At certain values of the field the metastable branch seems to cross different eigenvalue branches. These are in fact avoided crossings, which only become exact crossings at $T=0$. Consequently, the metastable branch does not consist of only one eigenstate, but is composed of a succession of eigenstates at different fields. For $T=0$, we can use the relation $-\ln \lambda_\alpha/(\beta N)=U_\alpha-M_\alpha H$ to calculate exactly the value of the magnetic field at which the m^{th} crossing involving the metastable branch occurs:

$$H_0 = 0, \text{ and } H_m = \frac{2J}{N-m}, \quad \text{with } m=1, \dots, N-1. \quad (43)$$

For the non-zero temperatures studied here, the field values of the avoided crossings involving the metastable branch deviate by at most 3% from their values at $T=0$. For $m=1$ and $m=2$ Eq. (43) corresponds to the definitions of H_1 and H_2 given in Sec. 3.2.

From Eq. (43), the number of avoided crossings in any neighborhood of $H=0$ is seen to go to infinity as $N \rightarrow \infty$. This is consistent with the existence of an essential singularity in the free energy at $H=0$ in the thermodynamic limit [18, 19, 20, 30, 31, 32, 33, 34, 35, 36, 37, 38, 39, 40, 41, 42, 43, 44]. In particular, it is reminiscent of the results of recent studies which found an essential singularity in the susceptibility at $H=0$ [42, 43, 44]. In that work the susceptibility was calculated in an ensemble in which the magnetization was restricted to negative values for positive fields. It was found that in the limit $H \rightarrow 0$, the singularity manifests itself through an infinite number of poles on the positive real axis, whose locations are given by $H \propto 1/n$, $n=1, 2, \dots, \infty$. However, there is specific disagreement between the values of the fields at which these poles occur and those corresponding to the avoided crossings in the TM spectrum. Since the TM eigenvalue crossings coincide with singularities in the metastable lifetimes recently found in rigorous low-temperature calculations [88], we believe the numerical discrepancy with Refs. [42, 43, 44] may be due to approximations used in that work.

Figure 3 shows the real parts (Fig. 3(a)) and the imaginary parts (Fig. 3(b)) of the constrained free-energy densities for $T/J=1.0$ and $N=8$. The composite branch corresponding to the metastable phase is marked by thick solid lines in both panels. The general features of the stable and metastable phases in Fig. 2(a) are reproduced in Fig. 3(a). For the real part of f_α the composite metastable branch is, except near the crossings, almost identical to the composite metastable branch in the eigenvalue spectrum, shown in Fig. 2(a). In the spectrum of the imaginary parts, the composite branch corresponding to the metastable phase consists of different lobes, each of which corresponds to a different eigenstate. The crossings for the metastable $|\text{Im}f_\alpha|$ correspond to avoided crossings in the eigenvalue spectrum of Fig. 2(a). Split lobes (such as the one at $H/J \approx 0.8$) occur when the metastable branch intersects branches from fans corresponding to more than two interfaces. Notice the extreme smallness of the values of the minima of the metastable $|\text{Im}f_\alpha|$, especially for weak magnetic fields, and how their range extends over roughly ten decades. We also observe, in accordance with our expectations for the finite-size scaling behavior of $|\text{Im}f_{\text{ms}}|$ outlined in Sec. 3.2, that the value of the metastable $|\text{Im}f_\alpha|$ at the first minimum is approximately given by the square of its value at $H=0$.

In order to avoid complications introduced by the mixing of two or more eigenvectors in the vicinity of the crossings (where, for example, the constrained magnetizations of the metastable eigenstates deviate appreciably from -1), we concentrate on the minima of $|\text{Im}f_\alpha|$, which are located away from the crossings. We denote the values of the fields at which these minima occur by H_m^{min} , such that $H_{m-1} < H_m^{\text{min}} < H_m$ for $m=1, \dots, N-1$ where H_m are the crossing fields of Eq. (43).

Figure 4 is a semi-log plot of only the metastable $|\text{Im}f_\alpha|$ vs. inverse field, J/H , for $N=9$ and $N=10$ at $T/J=1.0$. The thick straight line was drawn through the two minima for $N=10$ between

Table 1: The diameters of critical droplets, $2R_c(T, H)$, evaluated at (a) $H_1^{\min}(N)$, (b) $H_2^{\min}(N)$, and (c) $H_{N-1}^{\min}(N)$. Here N is the largest system size used at a particular field and temperature. At $H=H_{N-1}^{\min}(N)$ and for $T/J \geq 1.1$, the minimum of the metastable $|\text{Im}f_\alpha|$ was so shallow that we were unable to locate it.

(a)	T/J	$H_1^{\min}(N)/J$	$2R_c(T, H_1^{\min}(N))$	N
	0.4	0.330	6.0	6
	0.6	0.141	13.9	9
	0.8	0.084	22.3	10
	0.9	0.072	25.1	10
	1.0	0.064	27.1	10
	1.1	0.058	28.3	10
	1.2	0.054	28.6	10
(b)	T/J	$H_2^{\min}(N)/J$	$2R_c(T, H_2^{\min}(N))$	N
	0.4	0.309	6.5	8
	0.6	0.234	8.4	10
	0.8	0.231	8.1	10
	0.9	0.231	7.8	10
	1.0	0.228	7.6	10
	1.1	0.224	7.3	10
	1.2	0.224	7.0	10
(c)	T/J	$H_{N-1}^{\min}(N)/J$	$2R_c(T, H_{N-1}^{\min}(N))$	N
	0.4	1.838	1.1	9
	0.6	1.764	1.1	10
	0.8	1.723	1.1	10
	0.9	1.732	1.0	10
	1.0	1.781	1.0	10

$J/H=3.0$ and $J/H=4.0$, but, in accordance with Eq. (29), it also connects minima at smaller values of J/H for both $N=9$ and $N=10$. In agreement with our expectations outlined in Sec. 3.2 above, we find entirely different dependences on N and H for the metastable $|\text{Im}f_\alpha|$ in the weak-field and the intermediate-field regions. As is apparent from Fig. 4, for $H \geq H_3^{\min}$ $|\text{Im}f_\alpha|$ is independent of N . For $H \leq H_2^{\min}$, however, $|\text{Im}f_\alpha|$ depends strongly on N . This is further supported by Table 1, where we compare the diameter, $2R_c$, of the critical droplet with the system size, N , at three different values of the field, H_1^{\min} , H_2^{\min} , and H_{N-1}^{\min} . We find that for all temperatures studied, the size of the critical droplet exceeds N at H_1^{\min} , is comparable to N at H_2^{\min} , and is close to unity at H_{N-1}^{\min} . The quantity R_c was calculated from Eq. (38) using for σ_0 the exact equilibrium surface tension, $\sigma_{\text{eq}}(T)$, as obtained from Onsager's solution of the two-dimensional Ising model [81, 82, 85]. We also set $\Delta f = 2m_{\text{eq}}(T)H$, where

$$m_{\text{eq}}(T) = (1 - \text{cosech}^4 2\beta J)^{1/8} \quad (44)$$

is the exact zero-field equilibrium magnetization [93]. These identifications will be justified below.

The different dependences of the metastable $|\text{Im}f_\alpha|$ on N and H are discussed in more detail in the two subsections below.

4.1 The weak-field region

Figure 5 shows a semi-log plot of the metastable $N|\text{Im}f_\alpha|$ (plotted as $*$) and ξ_N^{-1} (shown as \circ) vs. N at $H=0$ and $T/J=1.0$. The dashed straight lines are guides to the eye drawn through the points at $N=9$ and $N=10$. The fact that these lines also approximately connect points at smaller values of N indicates that, in accordance with Eqs. (41) and (42), the metastable $|\text{Im}f_\alpha|$ and ξ_N^{-1} vanish exponentially with N .

The surface tension was calculated from either Eq. (41) or Eq. (42) by taking either the difference of the logarithms of the metastable $|\text{Im}f_\alpha|$ between two successive N or the difference of the logarithms of ξ_N^{-1} between two successive N . Taking into account appropriate correction terms arising from the N -dependent prefactors led to estimates for the surface tension that agree very well with $\sigma_{\text{eq}}(T)$, for both the metastable $|\text{Im}f_\alpha|$ and ξ_N^{-1} . Except for the lowest temperature studied (which is hampered by numerical underflow), the differences between our estimates and $\sigma_{\text{eq}}(T)$ are smaller than 2%, for both the metastable $|\text{Im}f_\alpha|$ and ξ_N^{-1} .

For the weak-field region, Fig. 6 shows a semi-log plot of the metastable $|\text{Im}f_\alpha|$ at H_1^{min} vs. N for all the temperatures studied. In accordance with Eq. (39), we find that the metastable $|\text{Im}f_\alpha|$ vanishes exponentially with N . The slopes of the straight lines in Fig. 6, divided by -2β , give an estimate for $\sigma(T, H)$ at the different temperatures.

We calculated $\sigma(T, H)$ by taking the difference of the logarithms of the metastable $|\text{Im}f_\alpha|$ in Eq. (39) at two different system sizes. In order to eliminate noticeable effects due to even-odd or odd-even pairs of system sizes, $\sigma(T, H)$ was obtained by using only odd-odd or even-even pairs of N . According to Eq. (43), the value of the field, H_1 , where the first crossing occurs, converges to zero in the limit $N \rightarrow \infty$. Therefore, $H_1^{\text{min}} < H_1$ also converges to zero, so that in the infinite-system limit, $\sigma(T, H)$ should converge to the equilibrium surface tension $\sigma_{\text{eq}}(T)$. Assuming linear convergence, three different values of $\sigma(T, H)$, as obtained from Eq. (39), are required in order to extrapolate $\sigma(T, H)$ to the infinite-system limit. Again, to avoid effects due to even-odd or odd-even combinations of system sizes, only the $\sigma(T, H)$ calculated from system sizes with the same parity were used to extrapolate $\sigma(T, H)$ to the infinite-system limit. The resulting extrapolations were then averaged to obtain an estimate of $\sigma(T)$ in the infinite-system limit. This procedure could not be carried out at $T/J=0.4$ due to numerical underflow for $N \geq 6$. Instead, the value of $\sigma(T)$ quoted at this temperature corresponds to $\sigma(T)$ as calculated directly from Eq. (39) using $N=4$ and 6.

In Fig. 7 we compare $\sigma(T)$ obtained from Eq. (39) (shown as \times) with the exact equilibrium surface tension, $\sigma_{\text{eq}}(T)$ (shown as the solid curve), for all the temperatures studied. Except for the lowest temperature, the agreement between the extrapolated result and $\sigma_{\text{eq}}(T)$ is excellent, indicating that our assumptions about the significance of $|\text{Im}f_\alpha|$ and about the shape of the critical excitation in the weak-field region are correct. It also suggests that in the thermodynamic limit the surface free energy of the critical excitation is given by the exact equilibrium surface free energy.

We tried to improve the estimates of $\sigma(T)$ by including various corrections. As an example, in Fig. 7 we also plot extrapolated results obtained from incorporating a bulk term of the form $-2H(N-1)$ in the exponential in Eq. (39) (shown as \square). The fact that we do not find universal improvement over the results obtained without corrections indicates that other terms besides a bulk term might be equally important. However, including various N - or H -dependent prefactors into Eq. (39) (as in Eq. (41) or Eq. (42)) separately or in conjunction with the bulk term did not consistently improve our previous results. These findings, together with the small difference between all our estimates, imply that the surface term in the free energy of the critical excitation is the dominant one.

Figure 8(a), where H_1^{\min} is plotted vs. N for various temperatures, shows that H_1^{\min} scales as

$$H_1^{\min}/J = c_1(T)N^{-\alpha(T)}. \quad (45)$$

Here $c_1(T)$ is a proportionality factor. The temperature dependence of the exponent $\alpha(T)$ is shown in Fig. 8(b). It is approximately two for $T/J=1.0$ and 1.2 and drops to a value below 1.5 for $T/J=0.4$. Since $H_1^{\min} \leq H_1$, according to Eq. (43), $\alpha(T) \geq 1$ for all temperatures. We also expect $\lim_{T \rightarrow T_c} \alpha(T) = 2$, corresponding to a correlation length that grows linearly with N at the critical temperature, in agreement with critical finite-size scaling theory [73]. However, neither the origin of the N dependence of H_1^{\min} , nor the detailed temperature dependence of the exponent $\alpha(T)$, is apparent to us at this time.

4.2 The intermediate-field region

A very different scaling behavior is found for $H_2^{\min} \lesssim H \lesssim 2J$. In this field interval, Fig. 4 indicates that the logarithm of the metastable $|\text{Im}f_\alpha|$ is independent of N . Only at fields $H \approx H_2^{\min}$ do we find some remaining finite-size effects, which are $\lesssim 3\%$. At stronger fields they vanish almost completely, becoming smaller than 0.1% . If, as we propose, the metastable $|\text{Im}f_\alpha|$ is related to the free energy of a critical droplet by Eq. (28), then this field interval of N -independent $|\text{Im}f_\alpha|$ should correspond to critical droplet sizes between N and unity. This was already seen in Tables 1(b) and 1(c). For all temperatures studied, we found that the diameter of the average critical droplet ranges from about eight lattice units for $N=10$ near the crossover field H_2^{\min} , down to one lattice unit for all N near $H/J=2$.

It can already be inferred from the thick straight line in Fig. 4 that the leading-order field dependence of the metastable $|\text{Im}f_\alpha|$ at intermediate fields can be described by Eq. (29) with an approximately field-independent value for the parameter Ξ . The slope of this line gives a rough estimate for Ξ , which was defined in Eq. (26). Below, we emphasize the lack of an H dependence in Ξ , $\hat{\Sigma}$, σ_0 , and m_{eq} by using the explicit notation $\Xi(T)$, $\hat{\Sigma}(T)$, $\sigma_0(T)$, and $m_{\text{eq}}(T)$.

In order to determine $\Xi(T)$, b , and $B(T)$ in a more systematic way, and thereby to study the validity of Eq. (29) for intermediate fields in greater detail, we performed linear least-squares fits on the logarithm of the minima of the metastable $|\text{Im}f_\alpha|$, excluding terms of order higher than two in the exponent. That leaves four independent parameters. However, assuming that $B(T)$ is independent of the field, it can be eliminated by differentiating $\ln |\text{Im}f_{\text{ms}}|$ with respect to the inverse magnetic field. With $|\text{Im}f_{\text{ms}}|$ as given in Eq. (29) and $d=2$, one obtains

$$\frac{d \ln |\text{Im}f_{\text{ms}}|}{d(1/|H|)} = - \left[\beta \Xi(T) + b|H| + O(H^2) \right]. \quad (46)$$

In order to utilize Eq. (46), we use the two-point finite-difference estimate for the derivative of $\ln |\text{Im}f_{\text{ms}}|$ based on the metastable $|\text{Im}f_\alpha|$ at two successive minima, H_m^{\min} and H_{m+1}^{\min} :

$$\begin{aligned} \frac{\Delta(\ln |\text{Im}f_\alpha|)}{\Delta(1/|H|)} &\equiv \frac{\ln |\text{Im}f_\alpha(H_m^{\min})| - \ln |\text{Im}f_\alpha(H_{m+1}^{\min})|}{1/|H_m^{\min}| - 1/|H_{m+1}^{\min}|} \\ &= - \left[\beta \Xi(T) + bH_{\text{eff}} + O(H^2) \right], \end{aligned} \quad (47)$$

with

$$H_{\text{eff}} \equiv \left| \frac{H_m^{\min} H_{m+1}^{\min}}{H_m^{\min} - H_{m+1}^{\min}} \right| \ln \left| \frac{H_m^{\min}}{H_{m+1}^{\min}} \right|. \quad (48)$$

We then perform three-parameter fits on $\Delta(\ln |\text{Im}f_\alpha|)/\Delta(1/|H|)$.

In the following, all the results reported for $\Xi(T)$ and b were obtained from three-parameter fits, whereas the results given for $B(T)$ were calculated from two-parameter fits with $\Xi(T)$ and b fixed. It should be emphasized, however, that since our results for $|\text{Im}f_\alpha|$ are numerically exact, we are using the least-squares method merely as a tool to determine the above parameters numerically. We have therefore assigned error bars such that χ^2 per degree of freedom is approximately unity.

Typical results of the three-parameter linear least-squares fits are shown in Fig. 9. The ratio $-\Delta(\ln |\text{Im}f_\alpha|)/\Delta(1/|H|)$ vs. H_{eff} is plotted at four different temperatures. The symbols represent the results obtained with the CTM method, except at zero field, where we plotted the numerically exact $\beta\Xi_{\text{eq}}(T)\equiv\beta\widehat{\Sigma}_{\text{eq}}^2(T)/(4\Delta m)$, with $\Delta m\equiv 2m_{\text{eq}}(T)$. Here $\widehat{\Sigma}_{\text{eq}}(T)$ was obtained by integrating numerically over the equilibrium droplet shape, which in turn was calculated by combining the Wulff construction with Onsager's exact zero-field anisotropic surface tension [81, 82]. The equilibrium magnetization $m_{\text{eq}}(T)$ is given by Eq. (44) above [93]. The solid curves represent our fits. The dashed straight lines start at the exact $\beta\Xi_{\text{eq}}(T)$ at zero field and have a slope of unity, corresponding to the value of $b=1$, expected from field theory, Eq. (30). It should be clear from Fig. 9 that our data in conjunction with the exact result at zero field can not be fitted by straight lines which would only involve b and $\Xi(T)$ as free parameters. The reason lies in the competition, in Eq. (29), between the $O(H^2)$ correction term in the exponential, which dominates for strong fields, and the prefactor, which becomes important for weaker fields. The accessible fields are sufficiently strong that the $O(H^2)$ -term is crucial and has to be included into the fits. Furthermore, the field at which the domination changes from one term to the other decreases as the temperature is lowered. That means that for lower temperatures, the range of fields we can cover does not extend as far into the region of weaker fields where the power-law prefactor dominates, as it does for the higher temperatures. This makes it increasingly difficult to obtain reliable estimates for the prefactor exponent b as T is lowered. In the intermediate-temperature region of $0.9\leq T/J\leq 1.1$, however, we find excellent agreement between the exact $\beta\Xi_{\text{eq}}(T)$ at zero field and the corresponding quantity obtained from our fits.

This agreement is further illustrated in Fig. 10. It shows $\Xi(T)$ divided by its equilibrium value, $\Xi_{\text{eq}}(T)$, vs. T , as obtained from three-parameter linear least-squares fits, including those shown in Fig. 9. For all $T/J>0.4$ these fits were performed on data corresponding to $N=10$. Due to numerical underflow, we were limited to a maximum system size of $N=9$ and fields $H\geq H_3^{\text{min}}$ for $T/J=0.4$. At temperatures $T/J\geq 1.1$, on the other hand, the minimum at H_{N-1}^{min} becomes so shallow that we were unable to locate it. That reduces the number of degrees of freedom in the fits for the higher temperatures, $T/J\geq 1.1$, by one as compared to the temperatures $0.6\leq T/J\leq 1.0$, making the fits for these temperatures slightly less reliable than the others. Two sets of data are shown. The data set corresponding to the diamonds was obtained from fits using all the discernible minima of the metastable $|\text{Im}f_\alpha|$ in the interval $H_2^{\text{min}}\leq H\leq 2J$. The data set corresponding to the crosses with error bars was obtained by excluding the minimum at H_2^{min} . (For clarity, the error bars for the diamonds, which are comparable to those for the crosses, are not shown.) This was done in order to illustrate the influence of uncontrollable finite-size effects due to competing critical excitations present in the metastable $|\text{Im}f_\alpha|$ at H_2^{min} . The largest finite-size effects occur at the higher temperatures $T/J\geq 1.1$. Corrections due to finite-size effects stay within the limits of the error bars for $T/J=0.8, 0.9$, and 1.0 and increase for both higher and lower temperatures. In the following, we always exclude from the fits the minimum of the metastable $|\text{Im}f_\alpha|$ that occurs at H_2^{min} .

The fits shown in Fig. 10 indicate that our results for $\Xi(T)$ are in excellent agreement with the hypothesis that the surface free energy of critical droplets is equal to that of equilibrium droplets of the same size at the same temperature, and that Δm equals twice the exact zero-field magnetization $m_{\text{eq}}(T)$. Except for $T/J=1.1$, we find agreement to within 10% between the estimated $\Xi(T)$ and

$\Xi_{\text{eq}}(T)$.

Independent confirmation of our results has been obtained by using Eq. (27) in conjunction with direct measurements of the lifetime of the metastable phase in Monte Carlo simulations [57, 58, 59, 60].

If we set $\Xi(T)$ to its equilibrium value $\Xi_{\text{eq}}(T)$, thereby reducing the three-parameter linear least-squares fit to a two-parameter fit, we obtain estimates for the exponent b , which are plotted in Fig. 11. As in Fig. 10, all the estimates were calculated for $H_3^{\text{min}} \leq H \leq 2J$ and $N=10$, except at $T/J=0.4$, where we used $N=9$. For $T/J > 0.8$ our results are consistent with $b=1$. Because of the aforementioned competition between the prefactor term, which involves the exponent b , and the $O(H^2)$ correction term in the exponential of Eq. (29), the estimates for b become less reliable at lower temperatures. As a result, we do not believe the large deviations of the estimate of b from unity for $T/J \leq 0.8$ to be physically meaningful. The general agreement of our estimates with $b=1$, in agreement with Eq. (30) and in disagreement with Eq. (31), confirm the importance of surface excitations on the critical droplet in determining the prefactor exponent b . Our results are fully consistent with previous numerical estimates [33, 37, 57, 79].

Figure 12 shows a comparison of $\Xi_{\text{eq}}(T)$, indicated by the solid line, with estimates for $\Xi(T)$ obtained from a two-parameter linear least-squares fit, in which b is fixed to 1. The droplet shape varies between a square at $T=0$ and a circle at $T=T_c$ (both shown for the whole temperature range by dashed lines). As in Fig. 10, we find close agreement between $\Xi(T)$ for the critical droplet with the corresponding value $\Xi_{\text{eq}}(T)$ for the equilibrium droplet. Together with Fig. 10, these results strongly support the notion that at a given temperature, the metastable phase decays through the formation of critical droplets having the same shape as equilibrium droplets at the same temperature. This also justifies the use of the exact equilibrium surface tension to estimate the size of the critical droplets in Table 1.

We also determined the prefactor $B(T)$ by reducing the four-parameter linear least-squares fit to Eq. (29) to a two-parameter fit by setting $\Xi(T)$ to its equilibrium value and $b=1$. Our results are displayed in Fig. 13 as \times with error bars. They are consistent with an exponential dependence of $B(T)$ on $1/T$, shown by the dashed line which was obtained from a weighted linear least-squares fit to our results. This temperature dependence of $B(T)$ can be obtained by adding an approximately temperature independent term ΔF to the free energy of the critical droplet. Our linear least-squares fit indicates that $\Delta F \approx 1.8$. This result is supported by a recent Monte Carlo study [59, 60]. Using continuum droplet theory, values of $B(T)$ were calculated from measurements of the lifetime of the metastable phase and are shown as \diamond with error bars in Fig. 13. They also follow a straight line with a value of $\Delta F \approx 1.2$ which is of the same order of magnitude as the CTM result. The discrepancy between the two estimates of ΔF is likely due to a temperature dependent kinetic prefactor in the Monte Carlo results. Also shown in Fig. 13 are values of $B(T)$ as calculated from the Becker–Döring droplet model by Harris [37]. Clearly, the Becker–Döring droplet model is inadequate to describe the temperature dependence of our results. An additive term in the free energy of the droplet was also found by Jacucci et al. [39] which they interpreted as a curvature-dependent surface free energy. However, although their additive term is field independent, it does depend on the temperature. Recent rigorous studies predict $\Delta F=4J$ at very low T [88, 89, 90, 91]. We note that our attempts at providing a simple, heuristic extrapolation of this result to the temperature range covered by the CTM and Monte Carlo studies by using $\Delta F(T) \approx 2\sigma(T)$ were not successful in fitting the numerical results. A clarification, especially of the physical origin of ΔF as found in the CTM and Monte Carlo results, must await further study.

For the interpretation of the results of the CTM method in terms of the droplet model to be consistent, the critical droplets have to be compact with well defined boundaries. Explicit verification of this is given in Appendix B.

5 Summary and Conclusions

We successfully applied the constrained-transfer-matrix method [45, 46] to the two-dimensional nearest-neighbor Ising ferromagnet in an external magnetic field to obtain complex-valued constrained free energies. In very good agreement with nucleation theory, we found several different field regimes, set apart by characteristic field and system-size dependences of the metastable $|\text{Im}f_\alpha|$. At $H=0$, we find that the metastable $|\text{Im}f_\alpha|$ is proportional to $(N\xi_N)^{-1}$ and therefore decays exponentially with N . For fields $0 < H < H_1$, where the size of the critical droplet as determined from droplet theory is larger than the transverse system size N , the decay of the metastable phase proceeds through the formation of “rod”-like excitations that extend $(N-1)$ lattice units in the finite direction and are only one lattice unit wide. Introducing a “surface tension” for nonzero fields, this again leads to an exponential decay of the metastable $|\text{Im}f_\alpha|$ with N . Due to the binding of two interfaces in the rod-like excitation, the argument of the exponential factor in the metastable $|\text{Im}f_\alpha|$ at $0 < H_1^{\text{min}} < H_1$ is approximately twice as large as the one at $H=0$. Extrapolating the nonequilibrium surface tension to the infinite system limit, we find very good agreement with Onsager’s exact equilibrium surface tension. For $H > H_2$, the decay of the metastable phase is dominated by critical droplets that are smaller than the finite width of the system. The metastable $|\text{Im}f_\alpha|$ in this field regime is therefore N -independent. The functional form of the imaginary part of the metastable free energy is the same as the one obtained from field-theoretical droplet models for infinitely large systems in ultraweak fields [20, 31] (see Eq. (29)). Also, our numerical results indicate that the critical droplets have the same surface free energy as equilibrium droplets of the same size at the same temperature. This and our estimates for the prefactor exponent b are in excellent agreement with series expansion [33, 34, 35, 36, 37], exact diagonalization [38], and Monte Carlo results [39, 40]. A residual N -dependence remains in the transition region $H_1 < H < H_2$, where a number of critical excitations of different shapes have comparable energies. Finally, in Appendix B, we have given some estimates for the field H_{MFSP} beyond which standard droplet theory is expected to become unreliable. For $H > H_{\text{MFSP}}$, we could not resolve a metastable imaginary free energy from all the other branches of $|\text{Im}f_\alpha|$.

Our results for the dependences of the metastable $|\text{Im}f_\alpha|$ on system size, field, and temperature can be compared with direct measurements of metastable lifetimes from Monte Carlo studies [22, 48, 49, 50, 51, 55, 56, 57, 58, 59, 60]. The picture that emerges from Ref. [57] involves four distinct field regions, in which the decay proceeds via different mechanisms. For very weak fields, the lifetimes obtained from the Monte Carlo simulations grow exponentially with the area of an interface cutting across the system, indicating that the excitations that lead to a decay of the metastable phase are of a size comparable to the finite dimension of the system. For intermediate fields, the lifetime is proportional to the inverse system volume, indicating that a small, size-independent nucleation rate is the rate-determining step. This “single-droplet region” [57] is characterized by decay via a single critical droplet. For yet stronger fields, the lifetime is size independent, indicating that the rate-determining process is the nucleation and growth of a finite density of droplets. This region was called the “multi-droplet region” in Ref. [57]. Finally, in the “strong-field region” beyond H_{MFSP} , the droplet picture becomes inadequate.

In the CTM study presented here, the “weak-field region”, where $|\text{Im}f_\alpha|$ depends exponentially on the system size, and the “intermediate-field region” correspond directly to the weak-field and the single-droplet regions found in the Monte Carlo study in Ref. [57]. In the CTM study the “weak-field region” extends from $H=0$ to approximately the field of the first eigenvalue crossing at H_1/J and the “single droplet region” extends from approximately H_1/J to approximately H_{MFSP} given in Appendix B, with no clearly distinguishable “multi-droplet region”. The values for H_{MFSP} obtained in the study presented here are of the same order of magnitude as the ones obtained by

Monte Carlo simulation [57].

Comparing the field and temperature dependence of $|\text{Im}f_\alpha|$ with that of the metastable lifetime from Monte Carlo calculations [57, 58, 59, 60] shows that for $H < H_{\text{MFSP}}$ both quantities can be obtained to leading order from the same droplet theory. The only difference is a kinetic prefactor that enters into the calculation of the lifetime [19, 20], which depends on the particular dynamic chosen in the Monte Carlo algorithm [57]. This is in complete agreement with and therefore supports the validity of Eq. (29) not only for ultraweak fields but also for intermediate fields.

Comparison of the results obtained for the typical short-range-force model, presented here, with CTM studies of two- and three-state systems with weak long-range interactions [45, 46, 61, 62, 63] clearly shows the differences and similarities in the properties of the metastable phase in the two types of systems [64]. The lifetime in short-range-force models becomes large but stays finite even in the thermodynamic limit, with an imaginary part of the metastable free energy that displays a droplet-model type essential singularity at zero magnetic field. Long-range-force models, on the other hand, exhibit metastable phases that become infinitely long-lived as the range of the interactions goes to infinity [15, 16], with an imaginary part of the metastable free energy that exhibits scaling behavior consistent with a well-defined non-zero spinodal field and a corresponding branch-point singularity [62, 63]. As the CTM studies for those systems show, the region in which the metastable $|\text{Im}f_\alpha|$ decays exponentially with N extends all the way out to the exactly known mean-field spinodal. Nevertheless, in both types of models, the leading-order dependence of the metastable $|\text{Im}f_\alpha|$ on the magnetic field and the temperature is, over a wide range of fields, given by a Boltzmann factor involving a well-defined free energy of formation for a critical excitation in the metastable phase [62, 63].

All our results strongly support the conclusion that the constrained-transfer-matrix formalism provides a nonperturbative method to numerically continue the equilibrium free energy into the metastable phase that, in contrast to the analytic continuations obtained in field-theoretical droplet models, does not rely on the explicit introduction of the particular excitations through which the metastable phase decays.

A question of current interest is whether or not the decay of metastability in anisotropic square-lattice Ising ferromagnets [94, 95] proceeds through equilibrium-shape critical droplets [81, 82, 88]. A study of this topic by the CTM method is in progress [96].

Acknowledgement

We would like to thank R. K. P. Zia for helpful correspondence and B. M. Gorman and J. Lee for useful conversations.

A The relationship between $|\text{Im}f_{\text{ms}}|$ and ξ_N at $H=0$

As may be seen from Fig. 3, the metastable phase for $|H| < H_1$ is represented by the eigenstate $|1\rangle$, so that $\text{Im}f_{\text{ms}} = \text{Im}f_1$ at $H=0$. Using Eqs. (17) through (20) one obtains

$$\text{Im}f_1 = -T\text{Im}S_1, \quad (49)$$

where S_1 is given by Eq. (19):

$$S_1 = -\frac{1}{N} \sum_{x_l, x_{l+1}} P_1(x_l, x_{l+1}) \text{Ln}\langle x_l | \lambda_1^{-1} \mathbf{T}_1 | x_{l+1} \rangle. \quad (50)$$

With Eqs. (12) and (16), it is easily shown that

$$\lambda_1^{-1}\mathbf{T}_1 = \lambda_1^{-1}\mathbf{T}_0 - |0\rangle \left(\frac{\lambda_0}{\lambda_1} - \frac{\lambda_1}{\lambda_0} \right) \langle 0|. \quad (51)$$

A term in the sum in Eq. (50) contributes to the imaginary part of S_1 only if the argument of the logarithm is negative. If we let Y denote the set of all configurations (x_l, x_{l+1}) such that $\langle x_l | \lambda_1^{-1}\mathbf{T}_1 | x_{l+1} \rangle < 0$, then for all $(x_l, x_{l+1}) \in Y$

$$\text{Im}(\text{Ln}\langle x_l | \lambda_1^{-1}\mathbf{T}_1 | x_{l+1} \rangle) = -i\pi. \quad (52)$$

Using Eqs. (49), (50) and (52) one obtains

$$\text{Im}f_1 = -\pi \frac{T}{N} \sum_Y P_1(x_l, x_{l+1}), \quad (53)$$

where \sum_Y denotes the sum over all configurations $(x_l, x_{l+1}) \in Y$. With Eqs. (10) and (51) this can be written as

$$\begin{aligned} \text{Im}f_1 = & -\pi \frac{T}{N} \sum_Y \langle 1 | x_l \rangle \\ & \times \left[\langle x_l | \lambda_1^{-1}\mathbf{T}_0 | x_{l+1} \rangle - \langle x_l | 0 \rangle \left(\frac{\lambda_0}{\lambda_1} - \frac{\lambda_1}{\lambda_0} \right) \langle 0 | x_{l+1} \rangle \right] \langle x_{l+1} | 1 \rangle. \end{aligned} \quad (54)$$

Using the definition of the correlation length in a system of finite width N , $\xi_N^{-1} \equiv \ln |\lambda_0/\lambda_1|$, and the fact that $\xi_N \rightarrow \infty$ for $T \rightarrow 0$, one obtains

$$\left(\frac{\lambda_0}{\lambda_1} - \frac{\lambda_1}{\lambda_0} \right) = 2 \sinh(\xi_N^{-1}), \quad (55)$$

so that

$$\begin{aligned} \text{Im}f_1 = & -\pi \frac{T}{N} \sum_Y \langle 1 | x_l \rangle \\ & \times \left[\langle x_l | \lambda_1^{-1}\mathbf{T}_0 | x_{l+1} \rangle - \langle x_l | 0 \rangle 2 \sinh(\xi_N^{-1}) \langle 0 | x_{l+1} \rangle \right] \langle x_{l+1} | 1 \rangle. \end{aligned} \quad (56)$$

The quantity in square brackets in Eq. (56) is simply $\langle x_l | \lambda_1^{-1}\mathbf{T}_1 | x_{l+1} \rangle$, and therefore negative for every (x_l, x_{l+1}) included in the sum. Since each of the terms in the difference inside the square brackets is positive, we must have

$$0 < \langle x_l | \lambda_1^{-1}\mathbf{T}_0 | x_{l+1} \rangle < \langle x_l | 0 \rangle 2 \sinh(\xi_N^{-1}) \langle 0 | x_{l+1} \rangle, \quad (57)$$

and consequently, since $\sinh(\xi_N^{-1}) = \xi_N^{-1} + O(\xi_N^{-3})$, we obtain

$$\text{Im}f_1 = \text{const} \frac{\pi T}{N} \xi_N^{-1} + O(\xi_N^{-3}) \propto (N \xi_N)^{-1}, \quad (58)$$

which yields Eq. (40). Only two exceptions to this scenario are possible. Exact cancellation of the leading-order terms in the square brackets for all $(x_l, x_{l+1}) \in Y$, or multiplicative factors of $O(\xi_N^{-1})$ arising from the matrix elements with the eigenvectors. Both effects are highly improbable and in any case would lead to an even smaller $|\text{Im}f_1|$ than that given by Eq. (58).

For $N=1$, \mathbf{T}_1 is a 2×2 matrix, so that we can easily calculate $\text{Im}f_1$ exactly, obtaining

$$\text{Im}f_1 = -\frac{\pi T}{2}(1 - e^{-\xi_1^{-1}}). \quad (59)$$

This gives $\text{const}=-1/2$ in Eq. (58). Under the assumption that the full transfer matrix of the system at $H=0$ and for $N>1$ can be approximated by an effective 2×2 transfer matrix with eigenvalues that are identical to λ_0 and λ_1 of the full transfer matrix [85, 86, 87], one would expect

$$\text{Im}f_1 \approx -\frac{\pi T}{2N}(1 - e^{-\xi_N^{-1}}), \quad (60)$$

leading to $\text{const} \approx -1/2$ for $N>1$ as well. In Fig. A.1 we plot $2N|\text{Im}f_1|/(\pi T \xi_N^{-1})$ as a function of N for all the temperatures studied. Our expectation is met for low temperatures and small system sizes. However, the plotted quantity still depends rather strongly on N and T for higher T and N . This is not so surprising, since for increasing T entropy terms also increase, and for increasing N the eigenvalue spectrum becomes more complex, both effects affecting the values of the matrix elements in the sum in Eq. (56).

We have observed that the quantity plotted in Fig. A.1 shows nice data collapse onto a single scaling function when plotted vs. the scaling variable $\sqrt{N-1}T$. However, we have not yet found a theoretical argument to support this empirical scaling relation.

B On the applicability of the compact-droplet picture

For the interpretation of the results of the CTM method in terms of the droplet model to be consistent, the critical droplets have to have well defined boundaries. This requires that the size of the critical droplets is larger than the single-phase correlation lengths in both the stable and metastable phases. A single-phase correlation length, ξ_{sp} , can be defined by

$$\xi_{\text{sp}}^{-1} = \ln \left| \frac{\lambda_\alpha}{\lambda_\beta} \right|. \quad (61)$$

For the single-phase correlation length corresponding to the stable phase, $\lambda_\alpha = \lambda_0$ is the dominant eigenvalue of the TM, whereas λ_β is given by the eigenvalues of the eigenstates that have magnetizations closest to $M=(N-2)/N$. In the case of the metastable phase, λ_α are the eigenvalues corresponding to the metastable branch in the eigenvalue spectrum, whereas λ_β are the eigenvalues corresponding to the branches with magnetizations closest to $M=-(N-2)/N$.

An estimate for the eigenvalues λ_α can be obtained analytically by using

$$\ln \lambda_\alpha \approx -\frac{N}{T} \text{Re}f_\alpha = -\frac{N}{T}(U_\alpha - M_\alpha H - T \text{Re}S_\alpha), \quad (62)$$

where U_α , M_α , and S_α are the constrained internal energy, constrained magnetization, and constrained entropy of the eigenstate $|\alpha\rangle$, as defined in Eqs. (17), (18), and (19). For low temperatures we can neglect the entropy term and approximate the internal energy and the magnetization by their values at $T=0$. We therefore insert $U_\alpha = -2J$, $U_\beta = U_\alpha + (4J/N)$, and M_α and M_β as given above into Eqs. (61) and (62). This yields:

$$\xi_{\text{st}} \approx \frac{T}{2(2J + H)} \quad (63)$$

$$\xi_{\text{ms}} \approx \frac{T}{2(2J - H)}. \quad (64)$$

Here ξ_{st} and ξ_{ms} denote the single-phase correlation length of the stable and the metastable phase, respectively.

Figure B.1 shows a comparison between the critical diameter, $2R_c$, and the single-phase correlation lengths, ξ_{st} and ξ_{ms} , for $T/J=1.2$. The solid lines were obtained from Eq. (38) for R_c and from Eqs. (63) and (64) for the single-phase correlation lengths. Also shown are the single-phase correlation lengths as obtained from TM calculations for $N=10$. For the stable single-phase correlation length the agreement between the TM results and Eq. (63) is excellent. In the case of the metastable single-phase correlation length the TM calculations agree well with Eq. (64) up to $H/J \approx 1$. For fields beyond $H/J \approx 1$, the increasing discrepancy between the metastable single-phase correlation length as obtained from the TM and Eq. (64), is caused by entropy effects and the deviation of U_α and M_α from their zero-temperature values.

An estimate for the magnetic field H_{MFSP} , at which standard continuum nucleation theory is expected to become suspect, is given by the intersection of ξ_{ms} and $2R_c$. An estimate of the temperature dependence of H_{MFSP} can be obtained by equating ξ_{ms} from Eq. (64) and $2R_c$ from Eq. (38). Using the exact zero-field equilibrium surface tension $\sigma_0^{\text{eq}}(T)$ and the equilibrium magnetization $m_{\text{eq}}(T)$ we get

$$\frac{H_{\text{MFSP}}(T)}{J} \approx \frac{4\sigma_0^{\text{eq}}(T)}{[2\sigma_0^{\text{eq}}(T) + Tm_{\text{eq}}(T)]}. \quad (65)$$

This relation is illustrated in Fig. B.2. As expected, $H_{\text{MFSP}}/J=2$ at $T/J=0$. However, since Eqs. (63) and (64) are low-temperature approximations, Eq. (65) must be unreliable as T approaches T_c . Certainly, continuum droplet theory breaks down when the diameter of the critical droplet becomes smaller than one lattice unit [88]. Using this condition one obtains H_{MFSP} as shown by the dashed line in Fig. B.2. The H_{MFSP} obtained from this condition is of the same order of magnitude as the one obtained from Eq. (65). Also plotted in Fig. B.2 (shown as \circ) is $H_{N-1}^{\text{min}}(T)$ for $N=10$ (from Table 1(c)) for all those temperatures that permitted us to determine it with the CTM method. Since $H_{N-1}^{\text{min}}(T)$ is the field at which according to Table 1(c) $2R_c \approx 1$, we expect it to be of the same order of magnitude as H_{MFSP} . This is indeed seen to be the case. The results summarized in this appendix confirm the applicability of the compact-droplet picture with sharp interfaces in the entire field and temperature range covered by our study.

References

- [1] J. E. McDonald. *Am. J. Phys.*, 30:870, 1962. Reprinted in Ref. [3].
- [2] J. E. McDonald. *Am. J. Phys.*, 31:31, 1963. Reprinted in Ref. [3].
- [3] F. F. Abraham. *Homogeneous Nucleation Theory*. Academic, New York, 1974.
- [4] D. W. Oxtoby. *J. Phys.: Condens. Matter*, 4:7627, 1992.
- [5] M. Gleiser and E. Kolb. In H. J. Herrmann, W. Janke, and F. Karsch, editors, *Dynamics of First Order Phase Transitions*, page 1, World Scientific, Singapore, 1992. This collection is also published as *Int. J. Mod. Phys. C*, **3**, No. 5, (1992).
- [6] J. Kripfganz. In H. J. Herrmann, W. Janke, and F. Karsch, editors, *Dynamics of First Order Phase Transitions*, page 11, World Scientific, Singapore, 1992.
- [7] W. Buchmüller and T. Helbig. In H. J. Herrmann, W. Janke, and F. Karsch, editors, *Dynamics of First Order Phase Transitions*, page 27, World Scientific, Singapore, 1992.
- [8] K. Kajantie. In H. J. Herrmann, W. Janke, and F. Karsch, editors, *Dynamics of First Order Phase Transitions*, page 149, World Scientific, Singapore, 1992.

- [9] M. Hackel, M. Faber, H. Markum, and M. Müller. In H. J. Herrmann, W. Janke, and F. Karsch, editors, *Dynamics of First Order Phase Transitions*, page 189, World Scientific, Singapore, 1992.
- [10] J. D. Gunton and M. Droz. *Introduction to the Theory of Metastable and Unstable States*. Springer-Verlag, Berlin, 1983.
- [11] J. D. Gunton, M. San Miguel, and P. S. Sahni. The dynamics of first-order phase transitions. In C. Domb and J. L. Lebowitz, editors, *Phase Transitions and Critical Phenomena, Vol. 8*. Academic, New York, 1983, and references cited therein.
- [12] K. Binder. *Rep. Prog. Phys.*, 50:783, 1987.
- [13] P. A. Rikvold and B. M. Gorman. In D. Stauffer, editor, *Annual Review of Computational Physics, Vol. I*. World Scientific, Singapore. In press.
- [14] L. S. Schulman. In V. Privman, editor, *Finite-Size Scaling and Numerical Simulation of Statistical Systems*. World Scientific, Singapore, 1990.
- [15] O. Penrose and J. L. Lebowitz. *J. Stat. Phys.*, 3:211, 1971.
- [16] O. Penrose and J. L. Lebowitz. In E. W. Montroll and J. L. Lebowitz, editors, *Fluctuation Phenomena*, chapter 5, page 293. North-Holland, Amsterdam, 1979.
- [17] G. Y. Sewell. *Phys. Rep.*, 57:307, 1980.
- [18] J. S. Langer. *Ann. Phys.*, 41:108, 1967.
- [19] J. S. Langer. *Phys. Rev. Lett.*, 21:973, 1968.
- [20] J. S. Langer. *Ann. Phys.*, 54:258, 1969.
- [21] C. M. Newman and L. S. Schulman. *J. Math. Phys.*, 18:23, 1977.
- [22] R. J. McCraw and L. S. Schulman. *J. Stat. Phys.*, 18:293, 1978.
- [23] V. Privman and L. S. Schulman. *J. Phys. A*, 15:L231, 1982.
- [24] V. Privman and L. S. Schulman. *J. Stat. Phys.*, 31:205, 1982.
- [25] C. M. Newman and L. S. Schulman. *J. Stat. Phys.*, 23:131, 1980.
- [26] G. Roepstorff and L. S. Schulman. *J. Stat. Phys.*, 34:35, 1984.
- [27] B. Gaveau and L. S. Schulman. *J. Phys. A*, 20:2865, 1987.
- [28] B. Gaveau and L. S. Schulman. *Lett. Math. Phys.*, 18:201, 1989.
- [29] A. F. Andreev. *Sov. Phys. JETP*, 18:1415, 1964.
- [30] M. E. Fisher. *Physics*, 3:255, 1967.
- [31] N. J. Günther, D. A. Nicole, and D. J. Wallace. *J. Phys. A*, 13:1755, 1980.
- [32] R. K. P. Zia. *Z. Phys. B*, 41:129, 1981.
- [33] M. J. Lowe and D. J. Wallace. *J. Phys. A*, 13:L381, 1980.
- [34] G. A. Baker, Jr. and D. Kim. *J. Phys. A*, 13:L103, 1980.
- [35] R. J. Baxter and I. G. Enting. *J. Stat. Phys.*, 21:103, 1979.
- [36] I. G. Enting and R. J. Baxter. *J. Phys. A*, 13:3723, 1980.
- [37] C. K. Harris. *J. Phys. A*, 17:L143, 1984.
- [38] C. J. Hamer. *J. Phys. A*, 16:1247, 1983.

- [39] G. Jacucci, A. Perini, and G. Martin. *J. Phys. A*, 16:369, 1983.
- [40] A. Perini, G. Jacucci, and G. Martin. *Surf. Sci.*, 144:53, 1984.
- [41] S. N. Isakov. *Commun. Math. Phys.*, 95:427, 1984.
- [42] D. B. Abraham and P. J. Upton. *Phys. Rev. Lett.*, 69:225, 1992.
- [43] D. B. Abraham and P. J. Upton. In H. J. Herrmann, W. Janke, and F. Karsch, editors, *Dynamics of First Order Phase Transitions*, page 299, World Scientific, Singapore, 1992.
- [44] D. B. Abraham and P. J. Upton. *Phys. Rev. Lett.*, 70:1567, 1993.
- [45] P. A. Rikvold. *Prog. Theor. Phys. Suppl.*, 99:95, 1989.
- [46] P. A. Rikvold. *Physica Scripta*, T38:36, 1991.
- [47] C. C. A. Günther, P. A. Rikvold, and M. A. Novotny. *Phys. Rev. Lett.*, 71:3898, 1993.
- [48] E. Stoll and T. Schneider. *Phys. Rev. A*, 6:429, 1972.
- [49] K. Binder and E. Stoll. *Phys. Rev. Lett.*, 31:47, 1973.
- [50] K. Binder and H. Müller-Krumbhaar. *Phys. Rev. B*, 9:2328, 1974.
- [51] E. P. Stoll and T. Schneider. *Physica*, 86–88B:1419, 1977.
- [52] K. Binder and M. H. Kalos. *J. Stat. Phys.*, 22:363, 1980.
- [53] W. Paul, D. W. Heermann, and K. Binder. *Europhys. Lett.*, 6:701, 1988.
- [54] H. M. Duiker and P. D. Beale. *Phys. Rev. B*, 41:490, 1990.
- [55] T. S. Ray and P. Tamayo. *J. Stat. Phys.*, 60:851, 1990.
- [56] H. Tomita and S. Miyashita. *Phys. Rev. B*, 46:8886, 1992.
- [57] P. A. Rikvold, H. Tomita, S. Miyashita, and S. W. Sides. *Phys. Rev. E*, 49:5080, 1994.
- [58] J. Lee, M. A. Novotny, and P. A. Rikvold. Unpublished.
- [59] M. A. Novotny. 1994. submitted to *Phys. Rev. Lett.*, preprint FSU-SCRI-94-48.
- [60] M. A. Novotny. Unpublished.
- [61] P. A. Rikvold, B. M. Gorman, and M. A. Novotny. *AIP Conf. Proc. Ser.*, 256:549, 1992.
- [62] B. M. Gorman, P. A. Rikvold, and M. A. Novotny. *Phys. Rev. E*, 49:2711, 1994.
- [63] T. Fiig, B. M. Gorman, P. A. Rikvold, and M. A. Novotny. *Phys. Rev. E*, 1994. in press, preprint FSU-SCRI-93-160.
- [64] B. M. Gorman and C. C. A. Günther. Numerical Studies of Metastability in Ising Systems: Short-range vs. Long-range Interactions. In D. P. Landau, K. K. Mon, and H. B. Schüttler, editors, *Computer Simulations in Condensed Matter Physics VII*, Springer-Verlag, Berlin. In press.
- [65] D. Stauffer, A. Coniglio, and D. W. Heermann. *Phys. Rev. Lett.*, 49:1299, 1982.
- [66] D. W. Heermann, A. Coniglio, W. Klein, and D. Stauffer. *J. Stat. Phys.*, 36:447, 1984.
- [67] T. S. Ray and J.-S. Wang. *Physica*, A 167:580, 1990.
- [68] D. Stauffer. In H. J. Herrmann, W. Janke, and F. Karsch, editors, *Dynamics of First Order Phase Transitions*, World Scientific, Singapore, 1992.
- [69] P. D. Beale. *Integrated Ferroelectrics*, 4:107, 1994.
- [70] C. Domb. *Adv. Phys.*, 9:149, 1960.

- [71] R. E. Blahut. *Principles and Practice of Information Theory*. Addison-Wesley, Reading, 1987.
- [72] J. N. Kapur and H. K. Kesavan. *Entropy Optimization Principles with Applications*. Academic, Boston, 1992.
- [73] M. P. Nightingale. In V. Privman, editor, *Finite-Size Scaling and Numerical Simulation of Statistical Systems*. World Scientific, Singapore, 1990.
- [74] W. H. Press, B. P. Flannery, S. A. Teukolsky, and W. T. Vetterling. *Numerical Recipes*. Cambridge Univ. Press, New York, 1992.
- [75] M. A. Novotny. Interpolation between dimensions. In M. Suzuki, editor, *Quantum Monte Carlo Methods in Equilibrium and Nonequilibrium Systems*, Springer-Verlag, Berlin, 1986.
- [76] K. Sekimoto. *Physica*, 135A:328, 1986.
- [77] K. Sekimoto. *Int. J. Mod. Phys. B*, 5:1843, 1991.
- [78] B. M. Gorman. Private communication. The value $(d-1)d/2=-1$ cited in [47] only contains the effect of the translational modes in the field theory [79].
- [79] D. J. Wallace. In M. Levy and J. C. Le Guillou, editors, *Phase Transitions*, Plenum, New York, 1982.
- [80] C. Rottman and M. Wortis. *Phys. Rev. B*, 24:6274, 1981.
- [81] R. K. P. Zia and J. E. Avron. *Phys. Rev. B*, 25:2042, 1982.
- [82] J. E. Avron, H. van Beijeren, L. S. Schulman, and R. K. P. Zia. *J. Phys. A*, 15:L81, 1982.
- [83] C. Rottman and M. Wortis. *Phys. Rep.*, 103:59, 1984.
- [84] M. Wortis. Equilibrium crystal shapes and interfacial phase transitions. In R. Vanselow, editor, *Chemistry and Physics of Solid Surfaces, Vol. VII*. Springer-Verlag, Berlin, 1988.
- [85] V. Privman and M. E. Fisher. *J. Stat. Phys.*, 33:385, 1983.
- [86] C. Borgs and J. Z. Imbrie. *Commun. Math. Phys.*, 145:235, 1992.
- [87] C. Borgs. In H. J. Herrmann, W. Janke, and F. Karsch, editors, *Dynamics of First Order Phase Transitions*, page 125, World Scientific, Singapore, 1992.
- [88] E. Jordão Neves and R. H. Schonmann. *Commun. Math. Phys.*, 137:209, 1991.
- [89] R. H. Schonmann. *Commun. Math. Phys.*, 147:231, 1992.
- [90] E. Scoppola. *J. Stat. Phys.*, 73:83, 1993.
- [91] E. Scoppola. *Physica A*, 194:271, 1993, and references cited therein.
- [92] M. A. Novotny, W. Klein, and P. A. Rikvold. *Phys. Rev. B*, 33:7729, 1986.
- [93] C. N. Yang. *Phys. Rev.*, 85:809, 1952.
- [94] R. K. P. Zia and D. J. Wallace. *Phys. Rev. B*, 31:1624, 1985.
- [95] R. Kotecký and E. Olivieri. *J. Stat. Phys.*, 70:1121, 1993.
- [96] C. C. A. Günther, P. A. Rikvold, and M. A. Novotny. In preparation.

Figure 2: (a) The eigenvalue spectrum, $-\ln \lambda_\alpha/(\beta JN)$, and (b) the constrained magnetizations M_α as given by Eq. (18), as functions of the magnetic field H/J for $T/J=1.0$ ($T/T_c \approx 0.441$) and $N=8$. Shown are only those branches that correspond to eigenstates that are symmetric under translation and reflection. The segments that contribute to the metastable branch are marked by thick lines.

Figure 3: (a) The real parts, $\text{Re}f_\alpha/J$, and (b) the imaginary parts, $|\text{Im}f_\alpha|/J$, of the constrained free energies vs. H/J , for $T/J=1.0$ and $N=8$. Notice the overall similarity of the stable and metastable branches of $\text{Re}f_\alpha/J$ to those of the eigenvalue spectrum in Fig. 2(a). The composite metastable branch is marked by thick lines. See detailed discussion in Sec. 4.

Figure 4: Semi-log plot of the imaginary parts of the constrained free energies, $|\text{Im}f_\alpha|/J$, that correspond to the metastable branch, shown vs. J/H . Plotted are data for two different system sizes, $N=9$ and $N=10$, at $T/J=1.0$. The thick, straight line was drawn through the two minima between $J/H=3.0$ and $J/H=4.0$ (marked by \bullet) for $N=10$ only.

Figure 5: Comparison of the metastable $N|\text{Im}f_\alpha|/J$ ($*$) and ξ_N^{-1} (\circ) vs. N in a semi-log plot at $H=0$ and $T/J=1.0$. The dashed straight lines are guides to the eye drawn through the points at $N=9$ and $N=10$. See details in Sec. 4.1.

Figure 6: Semi-log plot of the minimum of $|\text{Im}f_\alpha|/J$ at the weak field $0 < H_1^{\text{min}} < H_1$, plotted vs. N for $T/J=0.4, 0.6, 0.8, 1.0$, and 1.2 . At these weak fields, $|\text{Im}f_\alpha|$ decays exponentially with N as is evidenced by the straight lines. For each temperature, these lines were simply drawn through the points corresponding to the two largest system sizes available.

Figure 7: Comparison of extrapolations of the surface tension, $\sigma(T)/J$, as obtained from Eq. (39) (shown as \times), with the exact equilibrium surface tension, $\sigma_{\text{eq}}(T)$ (solid curve). Also shown (\square) are estimates obtained by adding a bulk term of the form $2H(N-1)$ in the exponential in Eq. (39). See detailed discussion in Sec. 4.1.

Figure 8: (a) Log-log plot of H_1^{min}/J vs. N for $T/J=0.4, 0.6, 0.8, 1.0$, and 1.2 . The straight lines show that H_1^{min} is proportional to $N^{-\alpha(T)}$. (b) The exponent $\alpha(T)$ as a function of T , as obtained from linear least-squares fits to our data.

Figure 9: Shown is a plot of the two-point finite-difference estimate for $\beta\Xi(T)/J$, $-\Delta(\ln|\text{Im}f_\alpha|)/\Delta(J/|H|)$, as a function of H_{eff}/J (compare Eqs. (47) and (48)) for four different temperatures. The symbols represent the results obtained with the CTM method, except at zero field, where we plotted $\beta\Xi_{\text{eq}}(T)/J$ obtained from the exact equilibrium quantities $\hat{\Sigma}_{\text{eq}}(T)$ and $\Delta m=2m_{\text{eq}}(T)$ as described in Sec. 4.2. The solid curves represent three-parameter linear least-square fits. The dotted straight lines have a slope of unity, corresponding to a value of $b=1$, and they intercept the vertical axis at the exact $\beta\Xi_{\text{eq}}(T)/J$.

Figure 10: The quantity $\Xi(T)$ divided by its equilibrium value $\Xi_{\text{eq}}(T)$, calculated from a three-parameter linear least-squares fit to Eq. (47). The \diamond correspond to results from fits including all the minima of the metastable $|\text{Im}f_\alpha|$ in the interval $H_2^{\text{min}} \leq H \leq 2J$, whereas the \times with error bars were obtained by excluding H_2^{min} to reduce uncontrollable finite-size effects. (For clarity, no error bars are shown for the \diamond .) The system size was $N=10$, except at $T/J=0.4$, where we used $N=9$. See Sec. 4.2 for a detailed discussion.

Figure 11: The prefactor exponent b vs. T/J . The values shown were obtained from a two-parameter linear least-squares fit to Eq. (47) by setting $\Xi(T)$ to its equilibrium value. See Sec. 4.2 for details.

Figure 12: The quantity $\Xi(T)/J^2$ as obtained from a two-parameter linear least-squares fit to Eq. (47), setting $b=1$. The solid line corresponds to the equilibrium value $\Xi_{\text{eq}}(T)$. The droplet shape interpolates between a square at $T=0$, given by $(2\sigma_0^2)/m_{\text{eq}}$, and a circle at $T=T_c$, given by $(\pi\sigma_0^2)/(2m_{\text{eq}})$, both of which are shown for the whole temperature range as dashed curves. The metastable CTM estimates, shown as \bullet with error bars, follow the equilibrium curve closely. The dashed vertical line marks the critical temperature. See Sec. 4.2 for details.

Figure 13: Semi-log plot of the prefactor $B(T)$ vs. inverse temperature J/T . The CTM results are indicated by \times with error bars and were obtained from a two-parameter linear least-squares fit to Eq. (29) by setting $\Xi(T)$ to its equilibrium value and $b=1$. The dashed line is a weighted linear least-squares fit of the values of $B(T)$ to the form $B(T)=k \exp(-\Delta F/T)$, and gives $\Delta F/J=1.78(5)$ and $k=2.12(7)$. Also shown are Monte Carlo results for $B(T)$ (\diamond with error bars) as obtained by continuum droplet theory from direct measurements of the lifetime of the metastable phase [59, 60]. The dot-dashed line is a weighted linear least-squares fit which gives $\Delta F/J=1.25(5)$ and $k=3.54(8)$. The \circ represent $B(T)$ as calculated from Becker–Döring droplet theory by Harris [37]. See Sec. 4.2 for details.

Figure .1: The quantity $2N|\text{Im}f_1|/(\pi T \xi_N^{-1})$ at $H=0$ as a function of N is shown for all the temperatures studied. At $T/J \leq 0.8$ numerical underflow prevented us from obtaining reliable results for the larger N . An exact calculation of $2N|\text{Im}f_1|/(\pi T \xi_N^{-1})$ at $H=0$ for $N=1$ leads to a value of unity for all temperatures (shown as \bullet). See Appendix A for more details.

Figure .1: Comparison of analytical estimates of the diameter of the critical droplet, $2R_c$, with the estimated single-phase correlation lengths, ξ_{st} for the stable phase, and ξ_{ms} for the metastable phase at $T/J=1.2$. Here $2R_c$ was calculated from Eq. (38), and ξ_{st} and ξ_{ms} were obtained from Eqs. (63) and (64). The transfer-matrix results for ξ_{st} and ξ_{ms} for $N=10$ are shown as \diamond .

Figure .2: Estimates of the crossover field H_{MFSP}/J obtained from Eq. (65) (solid line) and from the condition $2R_c=1$ (dashed line). Also plotted (\circ) is $H_{N-1}^{\text{min}}(T)/J$ for $N=10$, the field corresponding to the minimum of the metastable $|\text{Im}f_\alpha|$ in the field interval $1 < H/J < 2$.